

Quantization-Aware Neuromorphic Architecture for Skin Disease Classification on Resource-Constrained Devices

Haitian Wang¹, Xinyu Wang¹, Yiren Wang¹, Bo Miao^{1*}, and Atif Mansoor¹

Department of Computer Science and Software Engineering,
The University of Western Australia (UWA), Perth, WA 6009, Australia

Abstract. On-device skin lesion analysis is constrained by the compute and energy cost of conventional CNN inference and by the need to update models as new patient data become available. Neuromorphic processors provide event-driven sparse computation and support on-chip incremental learning, yet deployment is often hindered by CNN-to-SNN conversion failures, including non-spike-compatible operators and accuracy degradation under class imbalance. We propose QANA, a quantization-aware CNN backbone embedded in an end-to-end pipeline engineered for conversion-stable neuromorphic execution. QANA replaces conversion-fragile components with spike-compatible transformations by bounding intermediate activations and aligning normalization with low-bit quantization, reducing conversion-induced distortion that disproportionately impacts rare classes. Efficiency is achieved through Ghost-based feature generation under tight FLOP budgets, while spatially-aware efficient channel attention and squeeze-and-excitation recalibrate channels without heavy global operators that are difficult to map to spiking cores. The resulting quantized projection head produces SNN-ready logits and enables incremental updates on edge hardware without full retraining or data offloading. On HAM10000, QANA achieves 91.6% Top-1 accuracy and 91.0% macro F1, improving the strongest converted SNN baseline by 3.5 percentage points in Top-1 accuracy, corresponding to a 4.0% relative gain, and by 12.0 points in macro F1, corresponding to a 15.2% relative gain. On a clinical dataset, QANA achieves 90.8% Top-1 accuracy and 81.7% macro F1, improving the strongest converted SNN baseline by 3.2 points in Top-1 accuracy, which corresponds to a 3.7% relative gain, and by 3.6 points in macro F1, corresponding to a 4.6% relative gain. When deployed on BrainChip Akida, QANA runs in 1.5 ms per image with 1.7 mJ per image, corresponding to 94.6% lower latency and 99.0% lower energy than its GPU-based CNN implementation. Source code is available at [Akida-Research-Project](#).

Keywords: Resource-Constrained Devices · Edge Computing · Neuromorphic Computing · Low Latency · Energy Efficiency

1 Introduction

Skin lesions include benign conditions and malignant disease, and timely recognition is essential for early intervention and appropriate referral. In Australia, melanoma is among the most frequently diagnosed cancers, with 10,600 cases in males and 7,600 cases in females in 2023 [2]. Cancer Council Australia further notes that Australia has one of the highest melanoma rates worldwide [6]. This

* Corresponding author

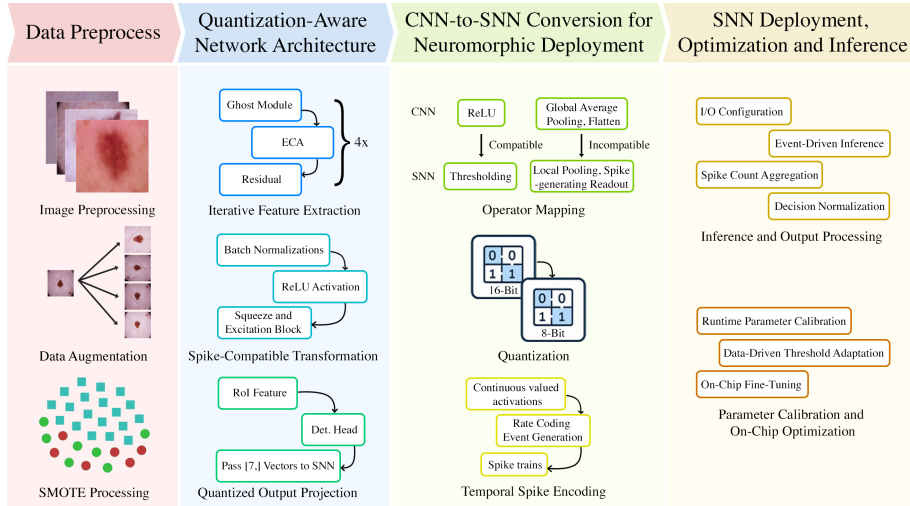


Fig. 1. End-to-end framework for quantization-aware neuromorphic skin lesion classification: (1) data preprocessing (quality filtering, augmentation, and SMOTE-based oversampling); (2) a quantization-aware network for feature extraction and spike-compatible transformation; (3) CNN-to-SNN conversion with operator mapping and temporal spike encoding; and (4) SNN deployment with on-chip optimization for real-time and energy-efficient inference on edge hardware.

high burden increases the number of lesions requiring assessment and amplifies the clinical cost of delayed detection and incorrect triage. Because melanoma can closely resemble benign lesions in dermatoscopic appearance, there is a practical need for portable decision-support systems that perform multi-class triage at the point of care and help distinguish melanoma from visually similar benign conditions. Although deep learning-based diagnostic systems have achieved strong performance [3], many deployments remain cloud-centric and require transferring sensitive patient data [43], which increases security risk [21] and is constrained by privacy regulation, including HIPAA [24] and GDPR [22]. For home and remote settings where connectivity and infrastructure are limited [16], practical systems must support on-device inference and efficient model adaptation without repeated cloud retraining.

Recently, Spiking Neural Networks (SNNs) and neuromorphic hardware have been explored for edge dermatological diagnosis [29]. SNNs encode information as spike events, enabling sparse and event-driven computation with low power consumption [10]. Their temporal coding can be effective in limited-label regimes [18]. Neuromorphic processors such as BrainChip Akida [5], IBM TrueNorth [4], and Intel Loihi [34] support SNN execution and on-chip incremental learning, allowing updates as new cases arrive [7]. Their compact form factor and reduced energy demand relative to GPUs further support portable, privacy-preserving deployment [14]. A common route to neuromorphic deployment is to train a conventional CNN backbone such as ResNet or DenseNet and convert it to an SNN for edge inference [33,27]. In practice, conversion is often brittle because standard CNN components such as BatchNorm and global pooling are not naturally

expressed in spike-based neuron operators, leading to operator substitution and calibration sensitivity [19]. Accuracy can further degrade on small, imbalanced medical datasets due to quantization effects and reduced capacity to preserve rare lesion cues [13].

We propose a Quantization Aware Neuromorphic Architecture (QANA) within the end-to-end pipeline as depicted in Fig. 1 to address these challenges. QANA consists of three modules. First, an iterative feature extraction and downsampling stage uses stacked Ghost blocks, spatially-aware efficient channel attention, and residual connections to reduce compute while preserving discriminative features required for dermatology. Second, a spike-compatible transformation stage applies quantization-aware normalization, bounded activations, and squeeze-and-excitation to produce activations suitable for spike encoding and hardware constraints. Third, a quantized projection head maps the compact representation to class logits in a form that remains compatible with CNN-to-SNN conversion and low-power neuromorphic execution.

On HAM10000, QANA achieves 91.6% Top-1 accuracy and 91.0% macro F1, improving the best converted SNN baseline by 3.5 points in Top-1 accuracy and 12.0 points in macro F1. On the clinical dataset, QANA attains 90.8% Top-1 accuracy and 81.7% macro F1, improving over the strongest baseline by 3.2 points in Top-1 accuracy and 3.6 points in macro F1. On BrainChip Akida, QANA processes an image in 1.5 ms at 1.7 mJ, yielding 94.6% lower latency and 99.0% lower energy than its CNN implementation on an RTX 3090.

The primary contributions of this research are as follows:

- We design QANA, a conversion-oriented quantization-aware architecture for dermatoscopic image classification that replaces conversion-fragile components with spike-compatible, bounded-activation blocks and lightweight attention to preserve discriminative features under 8-bit constraints.
- We formulate a graph-preserving CNN-to-SNN conversion pipeline for Akida that integrates BatchNorm reparameterization, uniform affine integer quantization, and deterministic operator lowering to ensure an all-integer executable spiking graph. Source code is available at [Akida-Research-Project](#).
- We develop a deployment and adaptation procedure on neuromorphic hardware that calibrates spike thresholds and integration windows and supports incremental updates by fine-tuning only the readout layer to accommodate domain shift without full retraining.

2 Related Work

Prior studies on neuromorphic hardware and Spiking Neural Networks (SNNs) have highlighted their suitability for edge inference and continual learning in constrained environments [18]. Platforms such as BrainChip’s Akida [5], IBM’s TrueNorth [4], and Intel’s Loihi [34] demonstrate ultra-low-power operation and support on-chip incremental learning, enabling model updates without full retraining. These features are advantageous for medical imaging tasks on edge devices. However, existing works primarily focus on general benchmarks like MNIST [26] or CIFAR [42] and rarely address domain-specific challenges in dermatology [36]. Furthermore, in medical image contexts, edge Spiking Neural

learning methods often suffer from catastrophic forgetting and fail to preserve performance on previously learned classes when new samples are introduced [17].

CNN-to-SNN conversion has become a common strategy to leverage mature CNN architectures, including ResNet and DenseNet, for deployment on neuromorphic processors [28]. Conversion toolkits, including Akida’s CNN2SNN [39], deliver compatibility by quantizing weights and replacing activation functions with spike-based equivalents. While some studies report preserved accuracy on standard datasets [35], performance significantly degrades on small or imbalanced medical datasets due to batching overfitting, quantization noise, and inability to capture rare lesion features [5]. Operations such as batch normalization and multi-bit activations require careful folding and scale management in integer-only conversion pipelines, and they are a frequent source of calibration error that can amplify performance loss on imbalanced medical data [41].

In parallel, conventional CNN-based methods, such as those using DenseNet-121 [8] or Inception-v4 [37], show high performance on benchmark datasets like ISIC. Despite their effectiveness, these models necessitate continuous retraining on cloud infrastructure to address domain shifts, new lesion types, or demographic variations [7]. Such retraining incurs latency, high computational cost, and data privacy concerns [25]. Moreover, general CNN models often fail to generalize to underrepresented conditions [30], such as rare tumors or images from diverse skin tones, highlighting the need for adaptive and privacy-preserving on-device solutions. These limitations motivate the development of neuromorphic frameworks that maintain diagnostic performance while supporting incremental learning and efficient operation in resource-constrained settings.

3 Methodology

This section details the complete pipeline for the development and deployment of the proposed neuromorphic skin lesion classification system. As shown in Fig. 1, the pipeline encompasses data preprocessing, the design of a quantization-aware neural network architecture compatible with spiking inference, conversion to an event-driven SNN format, and hardware-level deployment on the Akida platform.

3.1 Data Preprocessing

The pipeline includes three main stages: image preprocessing to ensure quality and compatibility with the Akida hardware, data augmentation to enhance dataset diversity and robustness, and SMOTE to address severe class imbalance among lesion categories.

Image Preprocessing All dermatoscopic images undergo automated integrity checks followed by a brief manual review. Inputs are processed at 64×64 to match the Akida on-chip memory budget used in our deployment. To retain lesion content at this resolution, we apply Grad-CAM on the pretrained backbone to obtain a coarse saliency map. A tight square crop is centered on the top-activated region and resized with antialiased area resampling to 64×64 . If the saliency peak lies within 10% of the image center or the saliency map is flat (coefficient of variation < 0.05), we fall back to a centered square crop. Pixel intensities are normalized per channel to $[0, 1]$. No denoising or inpainting is used. Cropping is computed per image without using class labels. The saliency

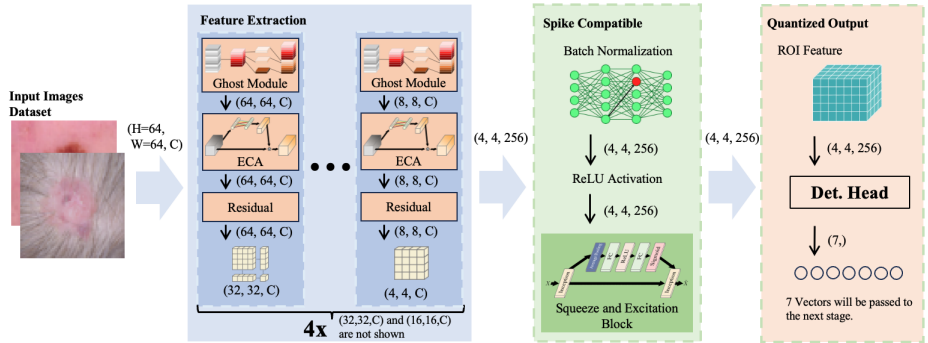


Fig. 2. Architecture of QANA. The backbone performs iterative feature extraction using stacked Ghost modules [11], spatially-aware efficient channel attention [40], and residual blocks. A spike-compatible transformation stage applies bounded activation and squeeze-and-excitation [12] before quantized projection to class logits.

model used to produce the Grad-CAM map is fixed before training, and the same cropping rule is applied to training, validation, and test images. This ensures that the preprocessing is deterministic given an input image and does not introduce split-dependent adaptation. For Grad-CAM generation we use a fixed ResNet-50 pretrained on ImageNet. This network is not fine-tuned on HAM10000 or the clinical dataset and is used only to produce a saliency prior for cropping. Since cropping depends only on the input image and a frozen saliency model, it does not use labels and it does not incorporate any information from validation or test outcomes.

Data Augmentation Augmentations preserve dermoscopic color cues. We use random horizontal and vertical flips (probability 0.5). Luminance is perturbed on the CIELAB L channel with a multiplicative factor in $[0.95, 1.05]$ or a gamma factor in $[0.97, 1.03]$. Contrast is adjusted in $[0.95, 1.05]$. No hue shift is applied. A gray-world normalization fitted on the training split is used during training only. All random draws use fixed seeds for reproducibility.

Synthetic Minority Oversampling (SMOTE) We perform SMOTE strictly in the learned embedding space rather than on raw pixels. For each training image x_i from class c , the backbone and spike-compatible transform produce a penultimate representation $\mathbf{r}_i \in \mathbb{R}^{4096}$ after global flattening. Let \mathcal{I}_c be the index set of class c and $\{\mathbf{r}_i\}_{i \in \mathcal{I}_c}$ the corresponding embeddings. Before neighbor search, embeddings are standardized on the *training split only* to avoid information leakage. A PCA whitening is then fitted on the same split and applied to stabilize distances in high dimension. Writing the sample covariance as $\Sigma = \mathbf{U}\Lambda\mathbf{U}^\top$ and retaining the top $d = 256$ components, the whitened vector is

$$\tilde{\mathbf{r}}_i = \Lambda_d^{-\frac{1}{2}} \mathbf{U}_d^\top (\mathbf{r}_i - \boldsymbol{\mu}), \quad (1)$$

where $\boldsymbol{\mu}$ is the training mean, $\mathbf{U}_d \in \mathbb{R}^{4096 \times d}$ the leading eigenvectors and $\Lambda_d \in \mathbb{R}^{d \times d}$ their eigenvalues. Nearest neighbors are computed with Euclidean distance in whitened space; for each $i \in \mathcal{I}_c$ we form a k -NN set \mathcal{N}_i with $k = 5$.

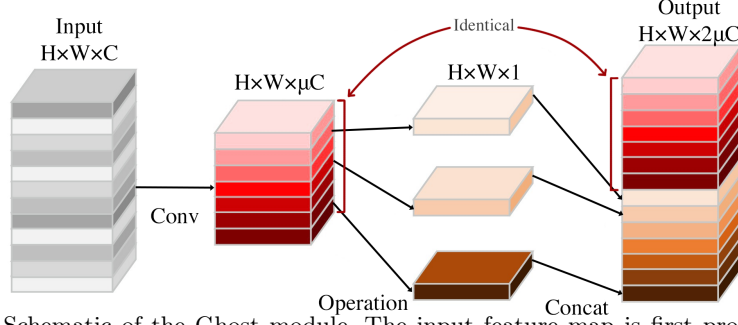


Fig. 3. Schematic of the Ghost module. The input feature map is first processed by a lightweight convolution to extract a reduced set of primary features with channel size μC , where C is the target output dimensionality and $\mu \in (0, 1)$ is a tunable ratio. Subsequently, inexpensive operations are applied to the primary features to generate additional ghost features of size $(1 - \mu)C$. These are concatenated along the channel axis to form the final output of size C .

To reduce the influence of outliers, we keep only “safe” minority anchors whose local median neighbor distance is below the class-specific 90th percentile:

$$\mathcal{S}_c^{\text{safe}} = \left\{ i \in \mathcal{I}_c \mid \text{med}_{j \in \mathcal{N}_i} \|\tilde{\mathbf{r}}_i - \tilde{\mathbf{r}}_j\|_2 \leq Q_{0.9} \left(\left\{ \text{med}_{j \in \mathcal{N}_u} \|\tilde{\mathbf{r}}_u - \tilde{\mathbf{r}}_j\|_2 \right\}_{u \in \mathcal{I}_c} \right) \right\}. \quad (2)$$

For each minority class c with $N_c = |\mathcal{I}_c|$ and $N_{\max} = \max_{c'} N_{c'}$, we synthesize to a target level τN_{\max} with $\tau = 0.85$ to avoid distribution collapse. The number of synthetic embeddings is

$$M_c = \max(0, \lfloor \tau N_{\max} - N_c \rfloor). \quad (3)$$

Each synthetic vector is generated from an anchor $i \in \mathcal{S}_c^{\text{safe}}$ and a random neighbor $j \in \mathcal{N}_i$ by a convex interpolation and a small, locally aligned perturbation to improve diversity. Let \mathbf{C}_i be the empirical covariance of $\{\tilde{\mathbf{r}}_u\}_{u \in \{i\} \cup \mathcal{N}_i}$, and let $\mathbf{U}_i^{(m)}$ contain its $m = 8$ principal directions. With $\delta_i = \text{med}_{j \in \mathcal{N}_i} \|\tilde{\mathbf{r}}_i - \tilde{\mathbf{r}}_j\|_2$ and $\sigma_c = 0.05 \text{ med}_{u \in \mathcal{I}_c} \delta_u$, we sample

$$\tilde{\mathbf{r}}_{\text{new}} = \tilde{\mathbf{r}}_i + \eta(\tilde{\mathbf{r}}_j - \tilde{\mathbf{r}}_i) + \sigma_c \mathbf{U}_i^{(m)} \boldsymbol{\xi}, \quad \eta \sim \mathcal{U}(0, 1), \quad \boldsymbol{\xi} \sim \mathcal{N}(\mathbf{0}, \mathbf{I}_m). \quad (4)$$

The synthetic embedding is then mapped back to the original feature space by the inverse whitening:

$$\mathbf{r}_{\text{new}} = \boldsymbol{\mu} + \mathbf{U}_d \boldsymbol{\Lambda}_d^{\frac{1}{2}} \tilde{\mathbf{r}}_{\text{new}}. \quad (5)$$

Synthetic data are *not* images. They are injected at the penultimate layer as additional feature vectors and used to train the quantized output projection with cross-entropy. During this stage the backbone up to the spike-compatible transform is frozen; only the classifier head is updated for 5 epochs with mixed real and synthetic embeddings. A subsequent short fine-tuning on real data re-enables the last block and the head to reconcile the feature distribution. Input images are still resized to 64×64 prior to feature extraction for hardware constraints, but no pixel-space mixing or image synthesis is performed at any time.

3.2 Quantization-Aware Network Architecture

As shown in Fig. 2, QANA follows a hierarchical design with four lightweight feature extraction stages and a spike-compatible transformation stage that produces

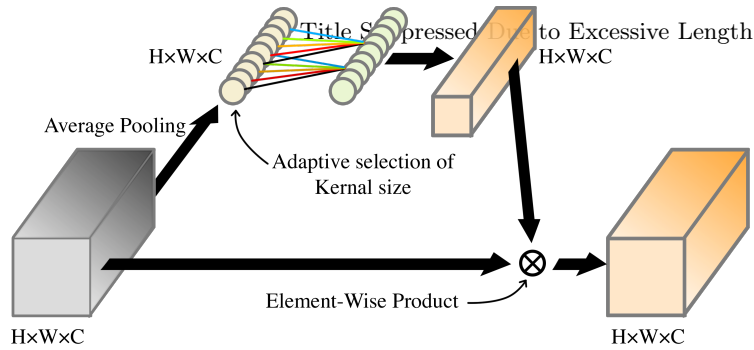


Fig. 4. Illustration of the Spatially-Aware ECA (SA-ECA) block. A depthwise convolution is applied to capture lightweight spatial-channel context, followed by batch normalization and a 1×1 pointwise projection to produce attention weights. The resulting weights rescale the input feature channels with minimal computational overhead.

SNN-ready activations for deterministic CNN-to-SNN conversion on Akida. The backbone prioritizes conversion stability by constraining activation ranges and by using operators that admit integer lowering, while preserving discriminative capacity through multi-scale feature generation and channel recalibration.

Backbone configuration. The input is $64 \times 64 \times 3$. The backbone contains four stages, each consisting of a Ghost block followed by BN, ReLU6, and a residual shortcut. Spatial downsampling is performed by 2×2 max pooling with stride 2 at the end of each stage, yielding a 4×4 feature map after stage four. When the shortcut changes the channel dimension, a 1×1 projection is used to match dimensions before residual addition. Dropout is applied only during training after the bounded activation to reduce overfitting on minority classes.

Iterative Feature Extraction and Downsampling Feature extraction is implemented as a stack of Ghost blocks [11] that expand representational diversity under a tight FLOP budget. For stage $l \in \{1, \dots, 4\}$, the input tensor $F^{(l-1)}$ is first mapped to a compact set of primary features using a pointwise projection. Additional features are then generated using depthwise transformations, and the two parts are concatenated to form the output feature map:

$$F_p^{(l)} = \mathcal{F}_{1 \times 1}^{(l)}(F^{(l-1)}), F_g^{(l)} = \mathcal{F}_{dw}^{(l)}(F_p^{(l)}), F_{ghost}^{(l)} = \text{Concat}(F_p^{(l)}, F_g^{(l)}). \quad (6)$$

In practice, the channel allocation between $F_p^{(l)}$ and $F_g^{(l)}$ follows the Ghost design ratio used in Fig. 3, ensuring that most computation is concentrated in the primary projection while the remaining channels are produced with depthwise operations. After feature generation, each stage applies BatchNorm followed by a bounded ReLU6 activation to keep post-activation values within a fixed and quantization-friendly range, then applies dropout for regularization. This bounded design reduces calibration sensitivity during 8-bit quantization and improves conversion robustness when activations are later encoded into spikes.

To model channel dependencies without introducing conversion-fragile global operators, each stage integrates a Spatially-Aware Efficient Channel Attention (SA-ECA) block inspired by ECA [40]. As illustrated in Fig. 4, SA-ECA replaces global pooling and 1D channel convolution with a depthwise spatial aggregation and a 1×1 projection that produces per-channel rescaling weights, followed

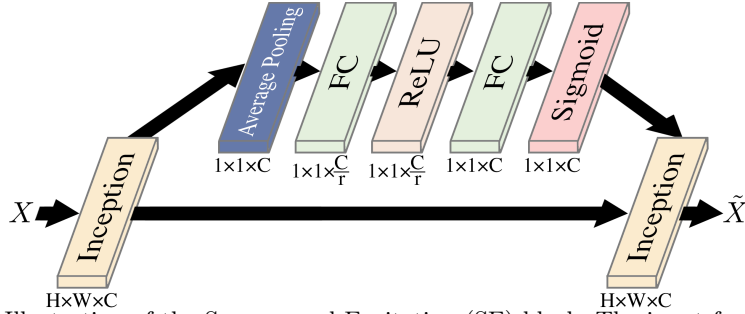


Fig. 5. Illustration of the Squeeze-and-Excitation (SE) block. The input feature map undergoes global pooling, followed by two fully connected layers with ReLU and sigmoid activations to compute channel-wise weights. The original feature map is then rescaled by these weights, enabling adaptive recalibration of channel responses.

by a sigmoid gate. The resulting weights modulate the stage features through channel-wise multiplication, yielding a lightweight attention mechanism that is compatible with integer operator lowering.

To maintain stable deep stacking in small-data regimes, each stage uses a residual shortcut with optional projection for dimension alignment, followed by spatial downsampling via max pooling. After four stages, the spatial resolution is reduced to 4×4 , producing a compact feature tensor suitable for spike-compatible transformation.

Spike-Compatible Feature Transformation The backbone output $F^{(4)}$ is passed to a spike-compatible transformation module designed for direct quantization and SNN integration. We first apply a SeparableConv2D ($3 \times 3, 256$) [31] to increase channel capacity while preserving hardware efficiency, then apply BatchNorm and an activation constraint that clips values into $[0, 1]$:

$$\hat{F} = \min \left(1, \max \left(0, \gamma_{\text{spk}} \cdot \text{BN}(\text{SepConv}_{3 \times 3, 256}(F^{(4)})) + \beta_{\text{spk}} \right) \right) \quad (7)$$

This bounded mapping aligns the activation range with spike encoding and avoids saturation under 8-bit affine quantization used in the subsequent conversion pipeline.

To further recalibrate channel responses, we apply a Squeeze-and-Excitation (SE) block [12] as shown in Fig. 5. The SE module computes channel-wise gates from global average pooled statistics using a two-layer bottleneck with a reduction ratio of 16, then rescales \hat{F} by the resulting sigmoid gates. This improves class sensitivity under imbalance while keeping the operator set compatible with the Akida conversion and lowering flow.

Quantized Output Projection Finally, the spike-compatible tensor is flattened to a vector $r \in \mathbb{R}^{4096}$ and projected to class logits through a linear readout:

$$\mathbf{y} = \mathbf{W}_{\text{cls}} r + \mathbf{b}_{\text{cls}}, \quad (8)$$

where $\mathbf{W}_{\text{cls}} \in \mathbb{R}^{7 \times 4096}$ and $\mathbf{b}_{\text{cls}} \in \mathbb{R}^7$. This projection is quantization-aware during training and produces logits in a form that is directly consumable by the CNN-to-SNN converter for neuromorphic inference.

3.3 CNN-to-SNN Conversion for Neuromorphic Deployment

We convert the trained quantization-aware CNN to an event-driven SNN with a graph-preserving flow that enforces an all-integer executable graph on Akida.

The conversion consists of (i) static reparameterization, (ii) 8-bit affine quantization, and (iii) deterministic operator lowering.

BN folding and activation constraint. All BatchNorm layers are folded into the preceding convolution or pointwise projection. For output channel c with convolution weights \mathbf{W}_c and bias b_c and BN parameters $(\gamma_c, \beta_c, \mu_c, \sigma_c^2, \epsilon)$, we use

$$\mathbf{W}'_c = \frac{\gamma_c}{\sqrt{\sigma_c^2 + \epsilon}} \mathbf{W}_c, \quad b'_c = \frac{\gamma_c}{\sqrt{\sigma_c^2 + \epsilon}} (b_c - \mu_c) + \beta_c. \quad (9)$$

Depthwise convolutions are folded channel-wise in the same manner. During training, non-supported nonlinearities are replaced by bounded ReLU6 so that post-activation ranges are fixed and compatible with spike encoding [15,32].

8-bit affine quantization. Weights and activations are quantized with uniform affine 8-bit fixed-point. For a real activation a and calibration-derived scale and zero-point (s_a, z_a) , the quantized value is

$$a_q = \text{clip}\left(\text{round}\left(\frac{a}{s_a}\right) + z_a, 0, 255\right), \quad a \approx (a_q - z_a) s_a. \quad (10)$$

For ReLU6-bounded activations, we set $z_a = 0$ and $s_a = 6/255$, which maps $[0, 6]$ to $[0, 255]$ without saturation. For layers constrained to $[0, 1]$, including Eq. 7, we set $z_a = 0$ and $s_a = 1/255$.

Spike emission. SNN inference uses an integrate-and-fire neuron with subtractive reset driven by integer activations. With membrane state u_t , integer drive a_q , and threshold τ , spike generation follows

$$s_t = \mathbb{I}(u_{t-1} + a_q \geq \tau), \quad u_t = (u_{t-1} + a_q) - \tau s_t. \quad (11)$$

Class scores are obtained from spike counts over the integration window, and Softmax is applied after spike integration [32].

Integer graph lowering and metrics. Supported operators are lowered deterministically to integer kernels, including convolution (standard, depthwise, separable), pooling, elementwise clipping, residual addition with scale alignment, and linear layers. For residual addition, the two integer tensors are brought to a common affine scale before summation. Given (s_1, z_1) and (s_2, z_2) , we choose a target scale $s_{\oplus} = \max(s_1, s_2)$ and rescale each branch by an integer multiplier and right shift so that both branches represent values under s_{\oplus} prior to addition. This prevents overflow and reduces drift introduced by mixed-scale accumulation. Spatial reductions are compiled as integer reductions with the division absorbed into output scaling, and reshape operations do not introduce compute. Any subgraph that requires floating-point dequantization is rejected. We report conversion success as $r_{\text{succ}} = 1 - |\mathcal{V}_{\text{fp32}}|/|\mathcal{V}|$, and quantify conversion-induced changes by $\Delta\text{Acc} = \text{Acc}_{\text{SNN}} - \text{Acc}_{\text{CNN}}$ and $\Delta\text{F1} = \text{F1}_{\text{SNN}} - \text{F1}_{\text{CNN}}$ on identical splits and preprocessing.

3.4 SNN Deployment, Optimization and Inference

The converted SNN model is deployed directly onto the BrainChip Akida neuro-morphic processor for hardware-based inference. The deployment process comprises several steps: loading the SNN model into the hardware runtime environment, configuring input/output data streams, and initializing internal buffers and neuron state registers.

Inference and Output Processing Inference is performed in an event-driven manner, with input images encoded into spike trains and propagated through the SNN in a fully parallel fashion. For each test or validation sample, the model outputs spike counts or firing rates at the final output neurons, corresponding to the target classes. To robustly map temporal spike responses to class probabilities, we aggregate the spike counts $S_c(t)$ for each class c within an integration window T , and apply a soft decision normalization:

$$\hat{p}_c = \frac{\exp\left(\alpha \sum_{t=1}^T w_t S_c(t)\right)}{\sum_{k=1}^C \exp\left(\alpha \sum_{t=1}^T w_t S_k(t)\right)} \quad (12)$$

where w_t is an optional temporal weighting factor (e.g., $w_t = \exp(-\beta(T-t))$ for decaying integration), α is a scaling parameter, and C is the number of output classes. Class prediction is then made as $\arg \max_c \hat{p}_c$.

In our implementation, we use uniform temporal weights $w_t = 1$ unless validation indicates a benefit from decaying integration. The scaling factor α is selected on the validation split and then fixed for the reported test evaluation.

Parameter Calibration and On-Chip Optimization After initial deployment, key runtime parameters, including output spike thresholds, integration windows, and temporal pooling parameters, are empirically calibrated on a held-out validation set. To further optimize the class assignment and suppress spurious events, a threshold adaptation can be formulated as:

$$\theta_c^* = \arg \min_{\theta} \left\{ \sum_{i=1}^N \mathbb{I}[y_i \neq \mathbb{I}(S_c^{(i)} > \theta)] \right\} \quad (13)$$

where $S_c^{(i)}$ is the total spike count for class c on sample i , y_i is the true label, and $\mathbb{I}[\cdot]$ is the indicator function. This allows data-driven threshold selection for each class. If performance deviation is observed relative to the original CNN, light on-chip fine-tuning is conducted using Akida’s incremental learning capability, adjusting only the last output layer to optimize for domain shift or quantization artifacts. For higher-detail cases, a 2×2 tiling fallback is triggered when $\max_c \hat{p}_c < 0.60$. Four overlapping 64×64 patches (20% stride overlap) are evaluated and logits averaged. On HAM10000, the trigger rate is 18%. All calibration, threshold selection, and optional on-chip fine-tuning steps use only the validation split. The test split is used only for final reporting and is not involved in any parameter selection.

4 Experiment

This section presents the datasets, experimental setup, and evaluation protocols, followed by detailed quantitative analyses of classification performance, ablation studies, and efficiency metrics under various deployment conditions.

4.1 Datasets

We used two datasets: the public HAM10000 benchmark and a proprietary clinical dataset from Nanjing Drum Tower Hospital, China. Both sets reflect a range of lesion types and clinical diversity.

Table 1. Class-wise precision, recall, F1 score of QANA on the HAM10000 test set.

Class	Precision	Recall	F1
Actinic keratoses	0.890	0.933	0.911
Basal cell carcinoma	0.890	0.901	0.896
Benign keratosis-like lesions	0.866	0.853	0.859
Dermatofibroma	0.925	0.976	0.950
Melanocytic nevi	0.887	0.817	0.851
Vascular lesions	0.949	0.966	0.957
Melanoma	0.956	0.933	0.944
Average	0.909	0.911	0.910

Table 2. Performance Comparison of Converted SNN Models on HAM10000

Model (SNN, Akida)	Top-1 Accuracy (%)	Macro F1 (%)
ResNet-50 [20]	85.7	76.4
DenseNet-121 [8]	86.5	77.2
Inception-v4 [37]	85.9	76.9
EfficientNet-B4 [23]	87.3	78.1
MobileNet-v2 [35]	83.4	74.7
SENet-154 [28]	86.9	77.8
Xception [9]	85.5	76.2
Multi-Scale Attention [30]	87.0	78.0
CNN Ensemble [1]	88.1	78.9
AKIDANet [5]	83.2	73.6
Ours	91.6	91.0

HAM10000 Dataset The HAM10000 dataset [38] consists of 10,015 dermatoscopic RGB images labeled by expert dermatologists into 7 categories: melanocytic nevus, melanoma, benign keratosis-like lesions, basal cell carcinoma, actinic keratosis carcinoma, vascular lesions, and dermatofibroma. The images originate from diverse sources and exhibit significant class imbalance. For all experiments, we adopted a standard 70%/10%/20% train/validation/test split.

Hospital Clinical Dataset A proprietary clinical dataset was established through a research collaboration with Nanjing Drum Tower Hospital, comprising 3,162 dermatoscopic images from 1,235 patients collected between June 2022 and February 2024 (Project No. NJG-2022-3233-CN). To ensure comparability with benchmark studies, lesion categories were curated to match the seven classes in HAM10000. Rare and unclassified conditions were excluded to maintain consistent labeling across classes. Each case was independently annotated by at least 2 board-certified dermatologists, with histopathological confirmation available for a subset of cases. All images and associated metadata were de-identified in accordance with ethics and governance requirements. Due to patient privacy, the dataset is not publicly released. Dataset partitioning followed a 70%/10%/20% train/validation/test split stratified by disease category. Splits were constructed to avoid patient overlap across training, validation, and test sets.

4.2 Experimental Setup

All model training, validation, and CNN-to-SNN conversion were conducted on a workstation with an Intel Core i9-12900K CPU, 128 GB RAM, and NVIDIA RTX 3090 GPU, running Ubuntu 22.04 LTS. The software environment included

Table 3. Per-image inference latency and energy consumption of all models on the HAM10000 test set. CNN baselines are measured on an NVIDIA RTX 3090 (GPU) and Intel i9-12900K (CPU); SNNs are measured on BrainChip Akida AKD1000. All values are averaged over 10,000 images. The rightmost columns show the percentage reduction achieved by SNNs on Akida compared to the corresponding CNN version.

Model	CNN (GPU)		CNN (CPU)		SNN (Akida)		Relative Reduction (%)	
	Latency (ms)	Energy (mJ)	Latency (ms)	Energy (mJ)	Latency (ms)	Energy (mJ)	Latency	Energy
ResNet-50 [20]	12.1	175.2	57.9	923.3	2.8	3.3	76.9	98.1
DenseNet-121 [8]	14.7	199.6	68.4	1075.2	3.1	3.5	78.9	98.2
Inception-v4 [37]	16.8	218.5	82.1	1237.5	3.5	4.1	79.2	98.1
EfficientNet-B4 [23]	18.9	242.1	93.6	1345.6	4.0	4.6	78.8	98.1
MobileNet-v2 [35]	6.9	97.5	68.2	1082.1	2.2	2.6	68.1	97.3
SENet-154 [28]	17.3	236.8	89.4	1312.4	3.8	4.4	78.0	98.1
Xception [9]	10.7	151.2	51.5	863.7	2.6	3.1	75.7	97.9
Multi-Scale Attention [30]	19.8	251.7	97.7	1391.5	4.2	5.0	78.8	98.0
CNN Ensemble [1]	36.1	450.5	157.2	2177.1	7.5	8.6	79.2	98.1
QANA (Ours)	27.6	163.1	83.9	841.5	1.5	1.7	94.6	99.0

Table 4. Ablation study of core modules in our model on the HAM10000 test set. Metrics are reported as percentages (%). Each row shows the incremental addition of modules. Inc. denotes fine-tuning of the readout layer after conversion using only validation data, while evaluation is performed on the fixed test split.

Configuration	Ghost	ECA	SE	Quant.	SMOTE	Inc.	Acc.	Rec.	Prec.	F1	AUC
Baseline							74.1	71.4	71.9	71.6	77.3
+ Ghost Block	✓						72.3	70.2	70.0	70.6	70.9
+ ECA	✓	✓					88.7	85.8	87.2	86.5	90.7
+ SE	✓	✓	✓				89.8	87.7	88.1	87.8	91.5
+ Augmentation	✓	✓	✓	✓			90.4	88.1	89.1	88.6	92.1
+ SMOTE	✓	✓	✓	✓	✓		91.0	89.2	90.0	89.6	92.7
+ Incremental Learning	✓	✓	✓	✓	✓	✓	91.6	90.7	91.2	91.0	93.4

Python 3.9, CUDA 11.8, TensorFlow 2.10, and Akida MetaTF SDK v2.2.1. Neuromorphic inference was performed on a BrainChip Akida AKD1000 PCIe board installed in the same system, with deployment and testing managed via the Akida Python API and default board settings.

4.3 Analysis of Classification Results on HAM10000 Dataset

Table 1 reports the class-wise precision, recall, and F1 score of QANA on the HAM10000 test set. Macro F1 is computed as the unweighted mean of per-class F1 scores on the test set. The model achieves consistent performance across lesion categories, including minority classes. With a Top-1 accuracy of 91.6% and a macro F1 of 91.0%, the system demonstrates effective discrimination of both common and rare lesions.

4.4 Classification Performance on HAM10000

To evaluate neuromorphic skin lesion classification under consistent deployment constraints, we trained a set of widely used CNN backbones and converted each model to an SNN using the same quantization-aware pipeline, then executed all converted networks on the same Akida platform with identical preprocessing and runtime settings. Table 2 summarizes the resulting Akida-SNN performance across canonical and advanced baselines, which typically exhibit reduced accuracy and macro F1 after conversion, with Top-1 accuracy spanning 83.2% to 88.1%. QANA attains 91.6% Top-1 accuracy and 91.0% macro F1 on HAM10000, yielding the best overall results under the same neuromorphic execution setting.

4.5 Inference Speed and Energy Consumption

We quantitatively evaluated inference latency and energy consumption against conventional CNN baselines and other converted SNN architectures. All SNN

Table 5. Performance comparison of converted SNN models on the Clinical Dataset.

Model (SNN, Akida)	Top-1 Accuracy (%)	Macro F1 (%)
ResNet-50 [20]	84.6	75.3
DenseNet-121 [8]	85.7	76.2
Inception-v4 [37]	85.2	75.8
EfficientNet-B4 [23]	86.3	77.0
MobileNet-v2 [35]	82.8	73.7
SENet-154 [28]	85.4	76.6
Xception [9]	84.2	74.8
Multi-Scale Attention [30]	86.5	77.2
CNN Ensemble [1]	87.6	78.1
AKIDANet [5]	81.9	71.5
Ours	90.8	81.7

models were deployed on the Akida AKD1000 PCIe board, while CNN baselines were tested on the NVIDIA RTX 3090 GPU and the Intel Core i9-12900K CPU. Latency is reported for batch size 1 with a fixed input pipeline, after a warm-up phase, and averaged over 10,000 images. Energy per image is computed as the mean device power during inference multiplied by the average per-image latency, using on-board power monitoring for Akida, NVIDIA-smi for GPU, and Intel RAPL for CPU. For each model, the reported inference latency corresponds to the average per-image processing time over 10,000 test samples. Energy consumption per image was measured as the mean device power during inference multiplied by the average inference time, using on-board power monitoring for Akida and NVIDIA-smi for GPU and Intel RAPL for CPU.

To ensure a fair and hardware-consistent comparison, all tested CNN architectures were converted to SNNs using our pipeline before deployment on Akida. Table 3 presents a comprehensive summary of inference latency and energy consumption across all evaluated models and platforms, as well as the relative reduction of these metrics for SNNs on Akida compared to their CNN GPU and CPU implementations. QANA achieves the lowest inference latency and energy consumption among the evaluated architectures. When deployed as an SNN on Akida, it processes an image in 1.5 ms and consumes 1.7 mJ, which corresponds to a 94.6% latency reduction and a 99.0% energy reduction relative to its CNN implementation on the RTX 3090.

4.6 Ablation Study of Model Components

Table 4 reports the ablation results on the HAM10000 test set, illustrating the contribution of each core module to the overall performance. Modules were incrementally enabled to measure their isolated and cumulative effects on classification metrics, including accuracy, recall, precision, F1 score, and AUC-ROC (%). The results demonstrate that each module provides consistent improvements, with the complete model achieving the highest accuracy and F1 score.

4.7 Classification Performance on Clinical Dataset

We evaluated the proposed neuromorphic skin lesion classification system and several representative CNN architectures, all converted to SNNs and deployed on the Akida hardware platform. Table 5 presents the Top-1 accuracy and macro F1 score for each model under the same deployment conditions. Our model achieves

the highest accuracy and macro F1 score among all tested methods, confirming its effectiveness and robustness for neuromorphic inference in clinical scenarios.

5 Conclusion

This paper presented QANA, a quantization-aware neuromorphic framework for on-device skin lesion classification. Experiments on HAM10000 and a real-world clinical dataset show that QANA maintains competitive diagnostic accuracy while enabling efficient SNN deployment on BrainChip Akida. On Akida hardware, the converted model achieves 1.5 ms per-image latency and 1.7 mJ per image, supporting real-time inference under strict energy and privacy constraints.

References

1. Amin-Naji, M., Aghagolzadeh, A., Ezoji, M.: Ensemble of CNN for multi-focus image fusion. *Inf. Fusion* (2019)
2. Australian Institute of Health and Welfare: Australia's health 2024: in brief. Tech. rep., AIHW (2024)
3. Bhatt, H., et al.: State-of-the-art machine learning techniques for melanoma skin cancer detection and classification: a comprehensive review. *Intell. Med.* (2023)
4. Borra, R.: Neuromorphic computing: bridging biological intelligence and artificial intelligence. *Int. J. Eng. Adv. Technol.* (2024)
5. Brátman, E., Dow, L.: Neuromorphic medical image analysis at the edge: on-edge training with the Akida BrainChip (2023)
6. Cancer Council Australia: Understanding melanoma (2025)
7. Chen, G., et al.: On-chip incremental learning based on unsupervised STDP implementation. In: *AICAS* (2024)
8. Chhabra, M., Kumar, R.: A smart healthcare system based on classifier DenseNet-121 model to detect multiple diseases. In: *Mobile Radio Commun. and 5G Netw.* (2022)
9. Chollet, F.: Xception: deep learning with depthwise separable convolutions. In: *CVPR* (2017)
10. Han, J.K., et al.: A review of artificial spiking neuron devices for neural processing and sensing. *Adv. Funct. Mater.* (2022)
11. Han, K., et al.: GhostNet: more features from cheap operations. In: *CVPR* (2020)
12. Hu, J., Shen, L., Sun, G.: Squeeze-and-excitation networks. In: *CVPR* (2018)
13. Hu, Y., Zheng, Q., Pan, G.: Fast-SNN: fast spiking neural network by converting quantized ANN. *IEEE Trans. Pattern Anal. Mach. Intell.* (2023)
14. Islam, R., et al.: Device and materials requirements for neuromorphic computing. *J. Phys. D: Appl. Phys.* (2019)
15. Jacob, B., et al.: Quantization and training of neural networks for efficient integer-arithmetic-only inference. In: *CVPR* (2018)
16. Janda, M., et al.: Early detection of skin cancer in australia: current approaches and new opportunities. *Public Health Res. Pract.* (2022)
17. Jenifer, P., Kannan, S.: Deep learning with optimal hierarchical spiking neural network for medical image classification. *Comput. Syst. Sci. Eng.* (2023)
18. Kim, E., Kim, Y.: Exploring the potential of spiking neural networks in biomedical applications: advantages, limitations, and future perspectives. *Biomed. Eng. Lett.* (2024)
19. Kim, Y., Chough, J., Panda, P.: Beyond classification: directly training spiking neural networks for semantic segmentation. *Neuromorph. Comput. Eng.* (2022)
20. Koonce, B.: ResNet-50. In: *Conv. Neural Netw. with Swift for TensorFlow* (2021)

21. Kourou, K., et al.: Applied machine learning in cancer research: a systematic review for patient diagnosis, classification and prognosis. *Comput. Struct. Biotechnol. J.* (2021)
22. Kretschmer, M., Pennekamp, J., Wehrle, K.: Cookie banners and privacy policies: measuring the impact of the GDPR on the web. *ACM Trans. Web* (2021)
23. Li, C., et al.: Improved EfficientNet-B4 for melanoma detection. In: *ICBAIE* (2021)
24. McGraw, D., Mandl, K.D.: Privacy protections to encourage use of health-relevant digital data in a learning health system. *NPJ Digit. Med.* (2021)
25. Moor, M., et al.: Foundation models for generalist medical artificial intelligence. *Nature* (2023)
26. Mu, N., Gilmer, J.: MNIST-C: a robustness benchmark for computer vision. *arXiv* (2019)
27. Muir, D.R., Sheik, S.: The road to commercial success for neuromorphic technologies. *Nat. Commun.* (2025)
28. Murugesan, G.K., et al.: Multidimensional and multiresolution ensemble networks for brain tumor segmentation. In: *MICCAI BrainLesion* (2019)
29. Nie, Y., et al.: Recent advances in diagnosis of skin lesions using dermoscopic images based on deep learning. *IEEE Access* (2022)
30. Qin, J., Bai, H., Zhao, Y.: Multi-scale attention network for image inpainting. *CVIU* (2021)
31. Rajabi, N., Kalhor, A., Iman-Eini, H.: A method for detecting and localizing open-circuit switch faults in MMCs using separable Conv2D neural networks. *IEEE Trans. Ind. Electron.* (2025)
32. Rueckauer, B., Lungu, I.A., Hu, Y., Pfeiffer, M., Liu, S.C.: Conversion of continuous-valued deep networks to efficient event-driven networks for image classification. *Front. Neurosci.* (2017)
33. Schuman, C.D., et al.: Real-time evolution and deployment of neuromorphic computing at the edge. In: *IGSC* (2021)
34. Scrofano, R., Davis, S.C., Taggart, J.L.: Radiation test performance of the Intel Loihi neuromorphic processor. In: *SCC* (2024)
35. Srinivasu, P.N., et al.: Classification of skin disease using deep learning neural networks with MobileNetV2 and LSTM. *Sensors* (2021)
36. Sun, X., et al.: A benchmark for automatic visual classification of clinical skin disease images. In: *ECCV* (2016)
37. Szegedy, C., et al.: Inception-v4, inception-resnet and the impact of residual connections on learning. In: *AAAI* (2017)
38. Tschandl, P., Rosendahl, C., Kittler, H.: The HAM10000 dataset: a large collection of multi-source dermoscopic images of common pigmented skin lesions. *Sci. Data* (2018)
39. Varadarajulu, S., et al.: Enhanced demodulator for 5g NTN using spatio-temporal attention convolutional autoencoder and Akida BrainChip SNN. In: *IET Conf. Proc.* (2024)
40. Wang, Q., et al.: ECA-Net: efficient channel attention for deep convolutional neural networks. In: *CVPR* (2020)
41. Xing, F., et al.: Homeostasis-based CNN-to-SNN conversion of Inception and residual architectures. In: *ICONIP* (2019)
42. Yang, J., et al.: OpenOOD: benchmarking generalized out-of-distribution detection. In: *NeurIPS* (2022)
43. Yaqoob, M.M., et al.: Symmetry in privacy-based healthcare: a review of skin cancer detection and classification using federated learning. *Symmetry* (2023)